



Urbanization-induced impacts on heat-energy fluxes in tropical South America from 1984 to 2020: The Metropolitan Area of Rio de Janeiro/Brazil



Vitor Fonseca Vieira Vasconcelos de Miranda ^{a,c,d}, Leonardo de Faria Peres ^{a,*}, Andrews José de Lucena ^b, José Ricardo de Almeida França ^a, Renata Libonati ^a

^a Department of Meteorology, Federal University of Rio de Janeiro (UFRJ), Campus Ilha do Fundão—Cidade Universitária, 21949-900, Rio de Janeiro, RJ, Brazil

^b Department of Geography, Agronomy Institute, Federal Rural University of Rio de Janeiro (UFRRJ), BR-465, Km 7, 23890-000, Seropédica, RJ, Brazil

^c Department of Earth Physics and Thermodynamics, Universitat de Valencia, 46100, Burjassot, Valencia, Spain

^d Earth Observation Unit, Portuguese Institute of Sea and Atmosphere, 1749-077, Lisboa, Portugal

ARTICLE INFO

Keywords:

MARJ
Urban heat island
Energy balance
SEBAL
Landsat

ABSTRACT

Our study aims to better understand the energy balance in tropical and wet climate urban areas by developing a 37-year (1984–2020) energy balance climatology based on SEBAL algorithm and Landsat data for Metropolitan Area of Rio de Janeiro (MARJ). Particularly, our results show that MARJ lost 13% of its vegetation cover and its urban area almost doubled since the 1980s decade. We show a positive (negative) urban-vegetation albedo (net radiation) difference in MARJ contributing to reduce the UHI intensity, but not capable to compensate for the warming effects related to the partitioning of latent and sensible heat fluxes. Our results revealed that the UHI intensity along the year in MARJ is maximum (minimum) during summer (winter) when the urban-vegetation temperature, sensible and latent heat fluxes absolute differences reach maximum values around 9.9°C (3.8°C), 150 Wm⁻² (71 Wm⁻²), and 330 Wm⁻² (145 Wm⁻²). We observe a great reduction of latent heat flux in urban areas in agreement with the pronounced effect of urbanization on wet climate regions. Thus, alternative/original strategies, not only based on increasing green areas, may be needed to reduce the urban warming in MARJ.

1. Introduction

According to the United Nations Development Programme, the world's urban population has increased from 751 million in 1950 to 4.2 billion in 2018. One in eight people already resides in 33 megacities, and projections show that by 2030 the world will have 43 megacities, most of them in developing regions [1]. Urban areas are regions where there is a widespread influence of humans on the natural environment, including changes in the local and regional climate. Extreme climate events, such as heatwaves and floods, are coupled with urban growth and expected to worsen due to climate change [2], challenging the implementation of an ambitious urban development agenda, that seeks to make cities and human settlements inclusive, safe, resilient, and sustainable [3].

Buildings and their materials have different thermal conductivity and capacitance characteristics, and their shape traps radiation and

pollutants, resulting in highly rough surfaces that affect airflow and diffusion dynamics [4]. Besides, engineering structures modify natural drainage networks by removing water from the surface and changing natural drainage regimes. The net effect is a profound change in the natural balance of momentum, mass, and energy. The main urban modifications affecting surface energy and radiation balance can be summarized as follows [5]: 1) the urban geometry promotes multiple reflection and radiation trapping leading to a greater absorption of incoming solar radiation, and therefore affecting the effective albedo [6, 7,8]; 2) the urban geometry and the increase in atmospheric pollutants promotes a greater retention of infrared radiation in the street canyon [9,10,11]; 3) buildings and pavements in cities increase heat absorption and delay heat release [12]; 4) most of the radiation absorbed by the urban surfaces is converted into sensible, rather than latent heat flux [13]; and 5) anthropogenic heat due to the energy used in human activities as urban transport, industrial processing, and domestic space

* Corresponding author. Departamento de Meteorologia, Instituto de Geociências (IGEO), Universidade Federal do Rio de Janeiro, Av. Athos da Silveira Ramos, 274, CCMN (Bloco G), Campus Ilha do Fundão—Cidade Universitária, 21949-900, Rio de Janeiro, RJ, Brazil.

E-mail address: leonardo.peres@igeo.ufrj.br (L. de Faria Peres).

heating/cooling the air [14].

Some works have recently studied the Metropolitan Area of Rio de Janeiro (MARJ) because of its fast development in the past years, becoming a region with more than 10 million people. For instance, MARJ has an urban heat island (UHI) phenomenon with tropical characteristics different from those in mid-latitude cities where the maximum UHI intensity occurs during the morning, and not at night as for the temperate cities [15].

Such peculiar UHI characteristic was a motivation for new studies about the effects of urbanization on the structure of the tropical urban atmospheric boundary layer in Rio de Janeiro. The comparison of a set of simulated tropical urban climates based on the tropical town energy budget (t-TEB) scheme against observed data supports UHI's morning occurrence in MARJ [16]. They concluded that such behavior results from the surface energy budget response to a high amount of solar radiation concurrently with intense evapotranspiration and low temperature of vegetated surfaces over a very wet soil layer. On the other hand, the use of remote sensing data (Landsat) relating land-surface temperature (LST) with land-cover classes helped to explain the thermal behavior over different surface types within the MARJ urban region and highlighted the importance to better understand the energy balance [17]. The daily and seasonal cycles of the global, direct, and diffuse solar radiation in MARJ were already characterized using in-situ data from 2011 to 2014 [18]. Data from MODIS LST products show that the maximum daytime surface urban heat island (SUHI) in MARJ occurs in February (7.9°C) and minimum in June (4.7°C), whereas for night-time, the maximum occurs in January (4.8°C) and minimum in July (3.4°C) [19]. Recently, Peres et al. (2018) [4] retrieved LST over MARJ from Landsat-5, 7, and 8 data, covering 32 years (1984–2015). They compared the LST evolution between 1984–1999 and 2000–2015 based on the Student's t-test and Mann-Whitney-Wilcoxon rank-sum-test, showing an LST increase in different areas since 1984 due to the urban expansion. This work has also computed the spatial variability of UHI intensity in MARJ, highlighting that the suburbs of underdeveloped countries, like Brazil, may reach LST values as high as the central city.

Most previous studies have focused on the temperature (air and surface) spatial and temporal behavior within MARJ. However, it is necessary to understand the implications of urbanization related to the energy balance fluxes since changes in sensible and latent heat fluxes are essential to trigger/amplify extreme events such as droughts, heatwaves, and severe thunderstorms. The knowledge of the energy balance is also fundamental to understand the UHI phenomenon and urban thermal behavior, and therefore, for designing strategies to mitigate it. Fortuniak (2003) [20] described that UHI and energy surface balance are well related. He showed that a numerical simple energy balance model reproduces singularities of the urban climate, and its outputs allow to estimate UHI intensity under specific meteorological conditions. Also, Lee et al. (2012) [21] enhanced that the energy balance can quantify the UHI intensity and cooling/heating effects. The knowledge of the energy balance is important not only as a proxy for climate extremes, but also to understand the heat exchange between urban and non-urban areas. Imhoff et al. (2010) [22] associated the UHI phenomenon with changes in surface properties, where the drainage system quickly removes most of the rainwater on impervious materials, and only a small portion of the net radiation goes for evaporation (latent heat flux). In contrast, most available radiation heats land-surface and the air directly above (sensible heat flux). Nevertheless, in-situ data of the energy balance components have low spatial representativeness because of the wide spatial variability of fluxes, and therefore measurements comprising the different surface types within MARJ are not available.

To our best knowledge, this is the first work that takes advantage of remote sensing data as a surrogate and complementary tool for capturing the seasonal and spatial variability of surface fluxes over MARJ. Here we apply the Surface Energy Balance Algorithm for Land (SEBAL) to compute the net radiation (Rn), sensible heat flux (H), latent heat flux (LE), and ground heat flux (G) based on Landsat data for a 37

years-period (1984–2020). Then, a monthly climatology of Rn, H, LE, G, and LST is developed to characterize the heat fluxes per land-cover type over MARJ. Finally, we establish an urban energy balance island intensity metric based on the monthly H, LE, Rn, G, and LST difference between the urban land-cover class and the remaining surface classes. The proposed work may improve Land Surface Models (LSMs) and the surface-atmosphere interaction processes representation, which is vital for numerical weather prediction and climate models. A common approach is to use satellite heat fluxes to validate LSMs to verify the consistency and robustness of the model outputs [23]. Regarding climate studies, our results may provide indicators for climate extremes, such as droughts and heatwaves, and a better comprehension of the UHI impacts and environmental public policies, which commit with the United Nations agenda.

2. Method and data

We describe in this section the study area, data, and methodology used in the present study. A flowchart showing a brief overview of the main sequential stages involved in the entire research is depicted in Fig. 1. It summarizes sections 3.1 to 3.6, which discuss in detail the steps outlined.

2.1. Study area

MARJ is located in the State of Rio de Janeiro, southeastern Brazil ($21^{\circ}17'S$, $40^{\circ}57'W$ and $23^{\circ}14'S$, $44^{\circ}53'W$). The Atlantic Ocean bathes MARJ, and it has two coastal bays, namely Guanabara and Sepetiba. Extratropical frontal systems, the South Atlantic Subtropical High (SASH), the South Atlantic Convergence Zone (SACZ), and humidity advection from the Amazon region (which is also related to SACZ) govern the Brazilian Southeast atmospheric dynamics. The maximum values of precipitation and mean daily temperature in MARJ occur during the austral summer; in contrast, the minimum ones occur in the austral winter [24,25,26]. In particular, the SACZ, an elongated convective band (clouds and precipitation), typically originating in the Amazon basin and extending toward southeast Brazil [24,27,28], has higher activity between October–March (wet-season) and occurrences in MARJ peaking in November–December. The SACZ is a significant climatological feature of the austral summer in southeast Brazil, and together with the convective activity in the Amazon basin, display a vital role in the South American Monsoon System (SAMS).

The MARJ encompasses 19 municipalities, namely: Belford Roxo, Duque de Caxias, Guapimirim, Itaboraí, Itaguaí, Japeri, Magé, Maricá, Nilópolis, Niterói, Nova Iguaçu, Paracambi, Queimados, Rio de Janeiro, São Gonçalo, São João de Meriti, Seropédica, Mesquita and Tanguá (Fig. 2).

During this decade, MARJ has undergone several changes in structure and urbanization, for example, the construction of the petrochemical complex of Rio de Janeiro (COMPERJ) and Itaguaí naval complex, including the Port of Itaguaí, Navy yard, naval base, and metal manufacturing plant for the construction of conventional and nuclear submarines, the 2014 FIFA World Cup in Brazil, the 2016 Olympic Games in Rio de Janeiro, among others. During structural changes, replacing naturally occurring vegetation and evaporating soil surfaces with impervious paving/building materials aggravates the UHI phenomenon by reducing latent heat flux and increasing sensible heat. Such land-surface transformations impact the local weather and climate of MARJ by changing circulation, turbulence, air dispersion, land-surface albedo, and the storage of heat due to evaporation and energy balance at surface [17,29,30,31].

2.2. Pre-processing

Here we compute the heat fluxes in the MARJ using remote sensing data from Thematic Mapper (TM), Enhanced Thematic Mapper Plus

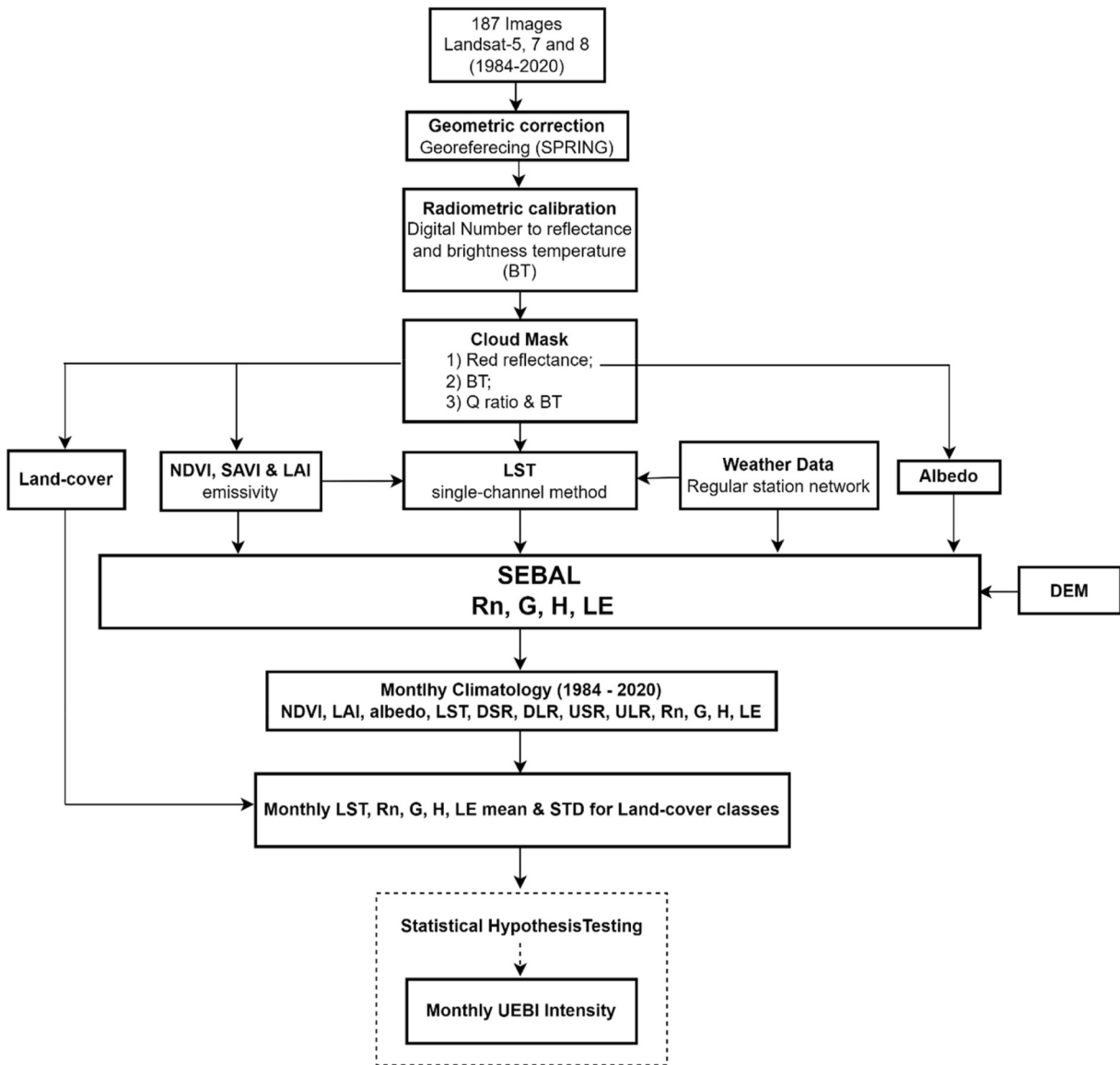


Figure 1. Flowchart showing the data used and the main stages involved in the entire research. Q is the ratio of near-infrared reflectance to red reflectance. LST, Rn, G, H, LE, DSR, DLR, USR, ULR, and STD stand for land-surface temperature, net radiation, ground flux, sensible flux, latent flux, downwelling shortwave radiation, downwelling longwave radiation, upwelling shortwave radiation, upwelling longwave radiation, and standard deviation, respectively. The statistical hypothesis tests are the t-test and the Wilcoxon-Mann-Whitney rank-sum test.

(ETM+), Operational Land Imager (OLI), and Thermal Infrared Sensor (TIRS) onboard Landsat-5, 7, and 8 satellites, respectively, obtained through the United States Geological Survey (USGS) [32]. A total of one hundred eighty-seven images from Landsat path/row 217/76 are used within the 37-year period from 1984 to 2020 (Fig. 3).

Raw images from Landsat-5 and 7 were georeferenced using the polynomial model first degree and nearest-neighbor interpolation in SPRING 4.3 [4], an open-source GIS and image processing software package developed by Brazilian National Institute for Spatial Research (INPE) [33]. Landsat Product Generation System [34] already provides Landsat-8 georeferenced images, but some images contain residual geolocation errors leading to expected sensor-to-sensor misregistration of 38m [35]. We georeferenced Landsat-8 images using the same baseline for TM and ETM + ones to maintain consistency, namely the Geocover_2003 dataset, a collection of standardized and orthorectified Landsat imagery covering MARJ.

The entire year of 2012 has no data available. Since May 31, 2003, the Scan Line Corrector (SLC), which compensates for the forward

motion of Landsat-7, has permanently failed, generating lines of gaps in the images as reported by USGS. Several studies developed methods and algorithms [36] to fill them in the data, but the gaps almost cover all the MARJ scenes and have a large variability. Thus, we did not consider Landsat-7 data after this time, whereas the Landsat-5 TM operational period ended by November 2011, and the launch of Landsat-8 in 2013 ensured the continuity of the data set.

We can observe in Fig. 3 a higher availability of images for the dry-season (April–September) than for the wet one (October–March), which is explained by the low cloud covering percentage in the data over the MARJ.

We have applied three cloud-masking algorithms to flag cloud contaminated pixels while maintaining image cloud-free pixels as much as possible around the study area [37,38]. The first one is a threshold value in the red band, which for the MARJ region we selected as 0.3 after several tests; the second one is a threshold value for brightness temperature (BT) in the thermal band that was set as 278 K. As the TIRS sensor has two thermal bands, the channel 10 (10,6–11,19 μm) was

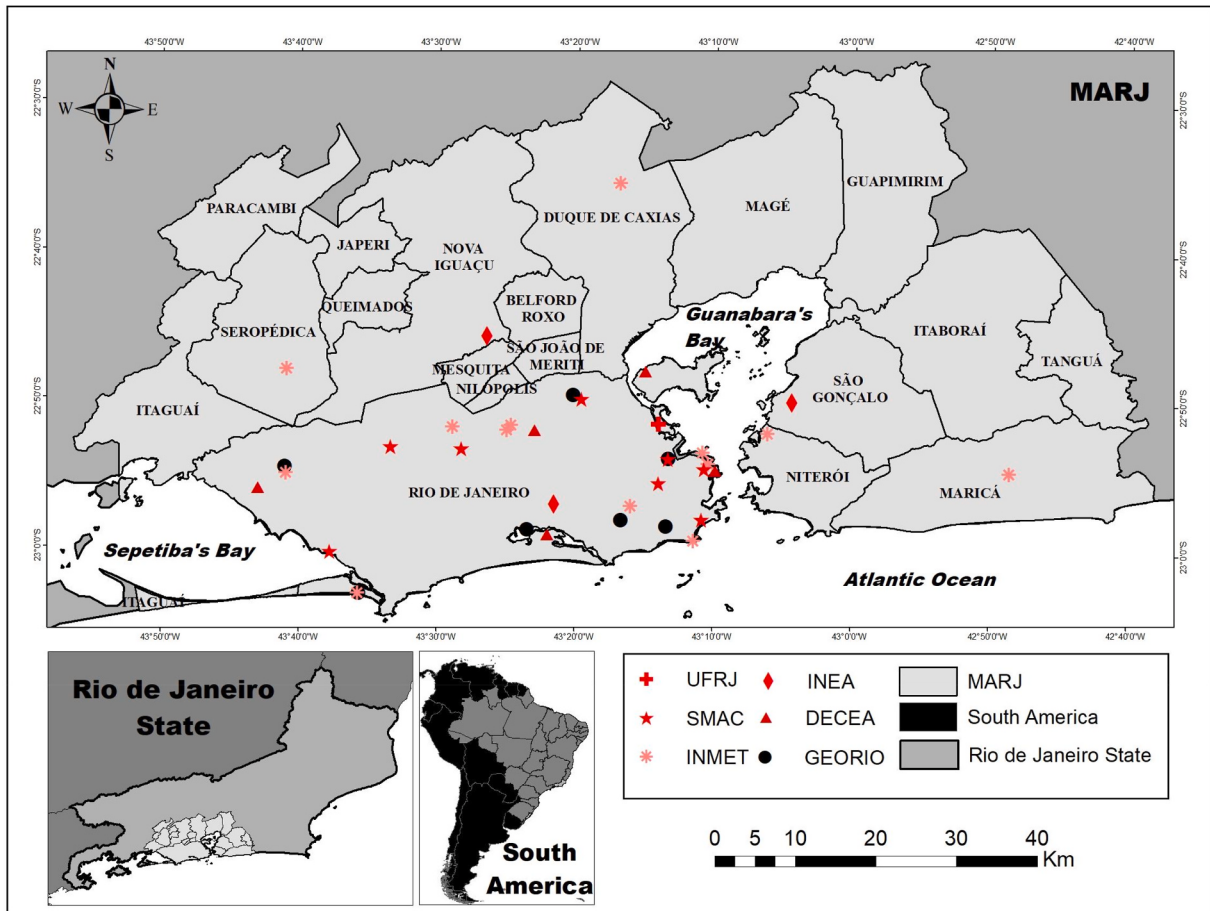


Figure 2. The location of the metropolitan Area of Rio de Janeiro (MARJ) and its 19 municipalities (light gray). The different symbols indicate the 37 weather stations' locations over MARJ, and the institutions responsible for operating each weather station network.

chosen, because of its similarity to TM and ETM+ (10,4–12,5 µm). The last one is the Q ratio method (near-infrared to red reflectance), close to unity for cloudy pixels, less than 0.8 for water, and greater than 1.6 for vegetation.

According to Roy et al. (2014) [39], the TIRS data show a bias of approximately 2% (band 10) and 4% (band 11) in absolute radiance when compared to indirect measurements from buoys in Lake Tahoe, Salton Sea, and deep oceans. Such bias translates to an overestimation of 2K–4K when expressed as a change in the apparent temperature of a 300K surface and exceeds the 2% accuracy requirements for TIRS. Stray light from beyond the nominal 15° TIRS field-of-view causes the bias, and there are studies for correcting it. Even so, works such as Yu et al. (2014) [40], Barsi et al. (2014) [41], and Wang et al. (2015) [42] indicate that the stray light effect is small in Band 10 but is more substantial in Band 11, and they suggest that the retrieval of LST should not use Band 11.

Accordingly, we have only considered the TIRS Band 10 to retrieve LST based on a single-channel method [43,44,45] that uses a correction factor for BT taking into account both the atmospheric and emissivity influence in the satellite signal [4,46]. This method performs a simplified atmospheric correction by using meteorological data from surface weather stations (air temperature and relative humidity) instead of atmospheric profiles and radiative transfer computations [4,43]. It is worth noting that applying a unique LST algorithm for all Landsat satellites guarantees LST consistency throughout the 36 years.

2.3. Meteorological dataset

The SEBAL algorithm requires in situ weather data (air temperature,

relative humidity, and wind speed) in order to compute the heat fluxes. In situ meteorological data are available from five different networks operated by the following agencies: Brazilian National Institute of Meteorology (INMET), Department of Airspace Control (DECEA); Rio de Janeiro State Environmental Institute (INEA), Municipal Environmental Secretariat (SMAC), and Geotechnical Institute Foundation of Rio de Janeiro (GEO-RIO). We also used data from a single station at Fundão Island operated by the Federal University of Rio de Janeiro (UFRJ) besides those from the agencies mentioned above, totaling 37 weather stations distributed over MARJ.

The symbols in Fig. 2 depict the 37 weather stations over MARJ and the agency responsible for operating each one. The weather stations are not regularly distributed over MARJ but concentrated in the city of Rio de Janeiro, whereas the vast majority of cities have only one or no stations. Some stations present discontinuities in the data, and the several operators differently register and distribute the meteorological information. The large part of the stations has hourly data, but others take observations solely at the synoptic hours of 0000, 0600, 1200, and 1800 UTC. We have considered observation at 1200 UTC for the last case, which is closest to the Landsat overpass. Meteorological data are available from all the 37 stations only between 2003 and 2009, covering 40 Landsat images used in this work (21.4%). Thus, we used a lower number of weather stations for years other than between 2003 and 2009, which may impact the characterization of the in situ meteorological data spatial variability. The lowest number of stations available over the 37-year study period is 12 covering 52 Landsat images (27%) between 1984 and 1997.

For each available Landsat image, we computed a simple spatial mean value of air temperature, relative humidity, and wind speed based

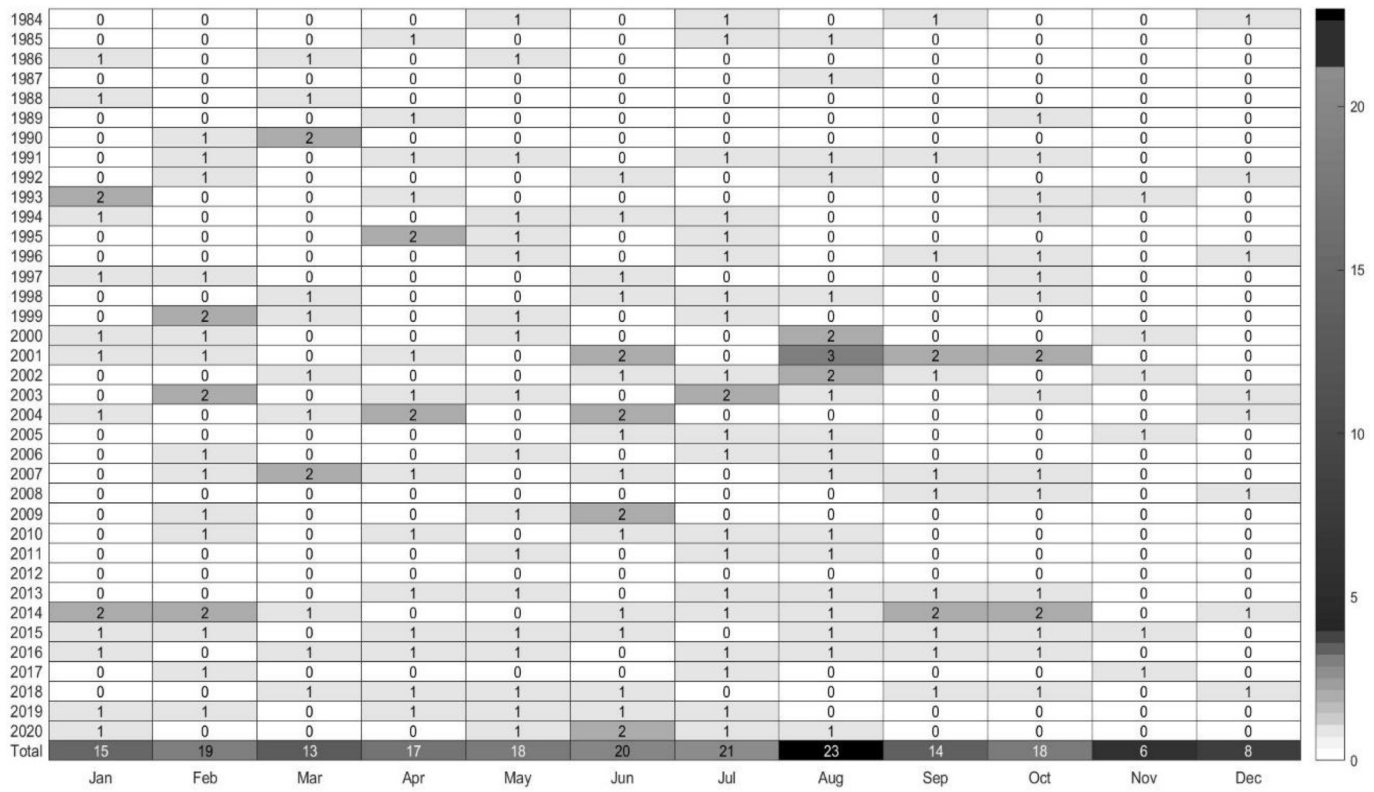


Figure 3. Monthly distribution for the number of Landsat images (path/row 217/76) used in this study covering the period from 1984 to 2020 covering MARJ.

on the weather stations observations closest to the time of satellite overpass, and used them as input to SEBAL.

2.4. SEBAL

SEBAL is a physically-based multi-step Surface Energy Balance Algorithm for Land [47] limited to clear sky conditions, which estimates the heat fluxes based on the energy balance closure according to equation (1), the energy balance equation, SEBAL main goal is to retrieve evapotranspiration as a residual of energy balance, but it can still be an essential tool to obtain the fluxes.

$$LE = Rn - G - H \quad (1)$$

Where LE is the latent heat flux, Rn is the net radiation, G is the ground heat flux, and H is the sensible heat flux. The term Rn is computed accordingly to equation (2), the radiation equation, as follows

$$Rn = (1 - \alpha) \times DSR \downarrow + DLR \downarrow - ULR \uparrow - (1 - \epsilon_0) \times DLR \downarrow \quad (2)$$

where α is the surface albedo, $DSR \downarrow$ is the downwelling shortwave radiation at the surface (Wm^{-2}), $DLR \downarrow$ is the downwelling longwave radiation at the surface (Wm^{-2}), and $ULR \uparrow$ is the upwelling longwave radiation leaving the surface (Wm^{-2}). In equation (2), we use a weighted average of reflectances (p_s) in Landsat bands together with the atmospheric transmittance ($\tau_{sw} = 0.75 + 2 \times 10^{-5} \times z$, where N is the terrain altitude) to compute the surface albedo (α). The $DSR \downarrow$ is obtained based on the solar constant (Gsc), the cosine of the solar zenith angle, the earth-sun distance (dr), and τ_{sw} . We compute the $DLR \downarrow$ using the Stefan-Boltzmann law for the air temperature (T_a) and an atmospheric emissivity value that is a function of the atmospheric transmittance ($\epsilon_a = 0.85 \times [-\ln(\tau_{sw})]^{0.09}$). The Stefan-Boltzmann law also computes $ULR \uparrow$ but uses the broad-band land-surface emissivity (ϵ_0) and temperature (LST). The emissivity ϵ_0 is obtained based on the Leaf Area Index (LAI), computed as described in SEBAL final manual [48] as a function of the

Soil Adjusted Vegetation Index [49], to avoid saturation of LAI when computed by NDVI.

We used data from the Topodata program of the National Institute of Space Research (INPE), a digital elevation model (DEM) at the national level, to consider the highly variable terrain altitude (N) of MARJ. The Topodata is based on data from the Shuttle Radar Topography Mission (SRTM) [50] provided by the USGS and has Landsat-like spatial resolution (30m).

SEBAL uses the Normalized Difference Vegetation Index [51], α , and Rn to compute empirically G , as described in equation (3), the ground heat flux equation.

$$G = [LST \times (0.0038 + 0.0074 \times \alpha) \times (1 - 0.978 \times (NDVI^4))] \times Rn \quad (3)$$

The estimate of H , equation (4), the sensible heat flux equation, uses the air density (ρ), the air specific heat at constant pressure (cp), the aerodynamic resistance to heat transport (rah), and the difference (dT) between the air temperature and the aerodynamic temperature.

$$H = (\rho \times cp \times dT) / rah \quad (4)$$

It is important to note that the knowledge of dT is usually challenging to obtain. SEBAL assumes a linear function of LST (i.e., $dT = aTs + b$) as a proxy of dT , and obtains the coefficients a and b by choosing two physically contrasting pixels on the image, namely the cold-pixel and the hot-pixel. The cold-pixel corresponds to a wet surface condition where the latent heat flux is maximum, and the sensible heat flux is zero. In this case, dT is zero, according to equation (4). Conversely, the hot-pixel is associated with a dry condition where the latent heat flux is zero, and the sensible heat flux is maximum. The hypotheses mentioned above result in a system with two equations and two unknowns, and therefore it is possible to calculate the coefficients.

Based on these principles, we choose the cold-pixel (hot-pixel) as the one with the lowest (highest) LST and highest (lowest) NDVI values. We followed Prasad (2012) [52] and selected an initial set of candidate pixels from the LST image based on the 1st (99th) percentile for the

cold-pixel (hot-pixel). We then use the NDVI value for each candidate to select the cold-pixel (hot-pixel) with the highest (lowest) NDVI value. Finally, we can compute H , in equation (5), the aerodynamic heat transport equation, by defining rah as follows

$$rah = [(\ln(z2 / z1)) / (u^* \times k)] \quad (5)$$

where $z2$ and $z1$ are heights in meters above the zero-plane displacement and the equation (5) represents the aerodynamic resistance for the neutral conditions values, in each case $z1$ represents the height for the surface and $z2$ is some distance above the zero plane displacement, but below the height of the surface boundary layer. Based on experienced analysis, SEBAL recommend $z2=2.0$ and $z1=0.1$, k is the Von-Karman constant (0.41) and u^* is the friction velocity, also for the neutral condition (ms-1). In spite of these calculations, the friction velocity must be one, where there is no effect of surface roughness, as described in equation (6), the friction velocity for neutral condition equation. For this, the air velocity is calculated at a blending height, with no effect of the surface features, defined as 200m:

$$u^* = [(u200 \times k) / (\ln(200 / zom))] \quad (6)$$

zom is the momentum roughness length, which can be approximated by an empirical relation with SAVI [48], equation (7), the momentum roughness length equation. The $u200$ is the wind speed at 200m, defined by the equation (8), the wind speed at 200m equation:

$$zom = \exp[-5,809 + (5.62 \times SAVI)] \quad (7)$$

$$u200 = \ln(200 / zom_1) \times (u^* \times 1 / k) \quad (8)$$

For the $u200$, a new friction velocity ($u^* \times 1$) and roughness length (zom_1) must be computed. zom_1 is given as a function of the vegetation height (h) associated with the pixel ($zom_1=0.123.h$). The $u^* \times 1$ needs as input, the ux which is the wind speed (ms-1) collected at the INMET stations along the MARJ at height zx , described in equation (9), the corrected friction velocity at stations height equation.

$$u^* \times 1 = [(ux \times k) / (\ln(zx / zom_1))] \quad (9)$$

The initial H value from equation (4) corresponds to a neutral stability condition and may not correctly represent the true sensible heat flux value. Such value works as an initial estimate of an interactive process where the Obukhov length (L), equation (10), the Obkhuv length equation, considers the stability condition for each pixel

$$L = -(\rho \times cp \times u^{*^3} \times LST) / (k \times g \times H) \quad (10)$$

where g is the acceleration due to gravity (9.81 ms-2), and H is the sensible heat flux obtained for a neutral stability condition according to equation (4). The lower atmospheric boundary layer is unstable if $L < 0$, stable if $L > 0$, and neutral if $L=0$. For unstable conditions, the stability correction factors for momentum (Ψ_m) and heat (Ψ_h) are calculated according to Paulson (1970) [53] and Webb (1970) [54]. Equations (11)-(16), the stability correction factors for momentum and heat under unstable conditions equations.

$$\begin{aligned} \Psi_{m(200m)} = & 2 \ln \ln \left(\frac{1 + X_{200m}}{2} \right) + \ln \ln \left(\frac{1 + X_{200}^2}{2} \right) - 2 \operatorname{ARCTAN}(X_{200m}) \\ & + 0,5\pi \end{aligned} \quad (11)$$

$$\Psi_{h(2m)} = 2 \ln \ln \left(\frac{1 + X_{2m}^2}{2} \right) \quad (12)$$

$$\Psi_{h(0,1m)} = 2 \ln \ln \left(\frac{1 + X_{0,1m}^2}{2} \right) \quad (13)$$

$$X_{200m} = \left(1 - 16 \frac{200}{L} \right)^{0.25} \quad (14)$$

$$X_{2m} = \left(1 - 16 \frac{2}{L} \right)^{0.25} \quad (15)$$

$$X_{0,1m} = \left(1 - 16 \frac{0,1}{L} \right)^{0.25} \quad (16)$$

Equations (17)-(19), the stability correction factors for momentum and heat under stable conditions equations, provide stability correction factors for stable conditions

$$\Psi_{m(200m)} = -5 \left(\frac{2}{L} \right) \quad (17)$$

$$\Psi_{h(2m)} = -5 \left(\frac{2}{L} \right) \quad (18)$$

$$\Psi_{h(0,1m)} = -5 \left(\frac{0,1}{L} \right) \quad (19)$$

The stability correction factors correct the friction velocity (u^*) and aerodynamic resistance to heat transport (rah) based on equation (20), the corrected friction velocity for stability equation, and equation (21), the corrected aerodynamic resistance to heat transport for stability equation.

$$u^* = (k \times u200) / \ln(200 / zom) - \Psi_m(200m) \quad (20)$$

$$rah = [\ln(Z2 / Z1) - \Psi_h(Z2) + \Psi_h(Z1)] / (u^* \times k) \quad (21)$$

Afterward, the iterative process runs continuously, correcting dT (hot), a and b coefficients, and the sensible heat flux H until dT (hot) and rah stabilize.

We have previously assessed the SEBAL's performance over MARJ [55] based on in-situ data from the MCITY project [56]. We used Landsat images as input to SEBAL and a micrometeorological station located at the Federal University of Rio de Janeiro. The project aimed to improve the energy balance knowledge over heterogeneous and urban areas and provided the first continuous in-situ measurement of heat fluxes over MARJ. The micrometeorological station worked between 2013 and 2014 with different sensors, such as a Net-Radiometer (Kipp & Zonen, CNR1), an Eddy Covariance System (Campbell, E150/CSAT), and two weather stations (Vaisala WXT520).

Although the validation procedure initially used two methods (Eddy Covariance and Bowen Ration), the eddy covariance results had different uncertainties (e.g., perturbations in the sensor, energy closure gap, extra energy due to the presence of advection from local circulation, and small non-detected eddies, and great sensibility on temporal averaging). In addition, during 2013–2014, we used only 10 Landsat images to validate SEBAL because of the presence of clouds, preventing a more robust statistical analysis. Although, we should interpret the findings from Miranda et al. (2018) [55] carefully, they indicated relative errors for the radiation balance components of 9% (5%) for downwelling (upwelling) longwave radiation and 9% (43%) for downwelling (upwelling) shortwave radiation, resulting in a relative error of 10% for the net radiation. The RMSE values were 39 Wm-2 (36 Wm-2) for downwelling (upwelling) longwave radiation and 63 Wm-2 (36 Wm-2) for downwelling (upwelling) shortwave. The best agreement for radiation fluxes was with upwelling longwave radiation, indicating accurate land-surface temperature retrievals. On the other hand, the upwelling shortwave radiation had the highest error, presumably associated with the surface albedo retrieval. Similar to the present work, we have considered the surface albedo as a simple weighted mean of the top-of-atmosphere reflectance in Landsat bands and did not account for the atmospheric and anisotropy effects. Respecting the turbulent fluxes,

the relative error and RMSE were respectively 30% (20%) and 70 Wm⁻² (68 Wm⁻²) for sensible (latent) heat flux.

Cheng et al. (2021) [57] conducted a more robust study providing a better idea of SEBAL performance. They derived a long time series of daily evapotranspiration in China with SEBAL and compared it with MODIS Evapotranspiration Product (MOD16). SEBAL results performed better than MOD16 against in-situ flux tower over subtropical zones in China, suggesting that SEBAL has a good performance for wet and hot climates (such as MARJ).

2.5. Land-cover maps

We derived a land-cover classification for MARJ based on Landsat data to analyze the heat fluxes behavior on different surfaces. The land-cover mapping uses a supervised classification from the Ecognition 8.9 software based on object-oriented language.

We chose a unique image representative for each decade (the 1980s, 1990s, 2000s, and 2010s): 07/11/1987, 10/01/1994, 08/01/2001, and 08/08/2013. Those selected images refer to a clear-sky condition.

The classification process initially uses an RGB composite of the representative dates (red, near-infrared, and shortwave-infrared bands) and then applies a multiresolution segmentation algorithm taking into account four parameters: 1) the weight of each band (1 for all bands); 2) scale parameter (50 fragments); 3) form parameter (0.1); and 4) compactness parameter (0.5). After segmentation, we collected pixel samples of 4 classes, namely water, vegetation, urban, and soil, and a classification algorithm was applied based on the nearest neighbor interpolation method between the segments resulting in four classes: urban, rural/urban-low-density, vegetation, and water.

2.6. Statistical approach for the urban energy balance island (UEBI) intensity

Here, we have used the UHI intensity concept to define a metric, named urban energy balance island (UEBI) intensity, that compares the H, LE, Rn, G, and LST monthly mean value of urban class (\underline{EB}_u) with the corresponding values of vegetation (\underline{EB}_v) and rural/urban-low-density (\underline{EB}_r) classes. For the LST parameter, the UEBI intensity is equivalent to the UHI intensity defined by Li et al. (2012) [59] and Peres et al. (2018) [4]. We have defined two UEBI intensity measures accordingly to the land-cover classes considered in this work:

$$\text{UEBI}_{EB_{(u-v)i}} = \underline{EB}_{ui} - \underline{EB}_{vi} \quad (22)$$

$$\text{UEBI}_{EB_{(u-r)i}} = \underline{EB}_{ui} - \underline{EB}_{ri} \quad (23)$$

where $\text{UEBI}_{EB_{(u-v)i}}$ is the UEBI intensity between urbanized and vegetated areas, $\text{UEBI}_{EB_{(u-r)i}}$ is the UEBI intensity between urban and urban-low-density classes, whereas the subscripts EB and i stand for the energy balance parameter (i.e., H, LE, Rn, G, or LST) and the months of the year. This arrangement yields 24 UEBI values per energy balance parameter (2 classes differences \times 12 months), allowing easy comparison between land-cover classes throughout the year and revealing the surface's role on the energy balance parameters. Each class's mean value only considers pixels below 100m to overcome the MARJ topography (lowlands and mountains) influence on the energy balance parameters.

We have tested all differences among land-cover classes based on the parametric two-sample *t*-test for the difference of means under the one-tailed hypothesis test (Wilks, 2006). The test was applied to differences between means under independence, considering unequal variances to examine whether the mean value of the balance parameter calculated from the urban class pixels is statistically different from other land-cover classes' corresponding mean value. We have also applied the non-parametric Wilcoxon-Mann-Whitney rank-sum test to examine the difference in location between the urban energy balance parameter samples and those from other land-cover classes. The null hypothesis is that

the two energy balance data batches have the same location.

3. Results and discussion

3.1. Land-cover maps

Fig. 4 shows land-cover maps for MARJ concerning the 1980s (a), 1990s (b), 2000s (c), and 2010s (d) decades. The classification considers four classes: urban, rural/urban-low-density, vegetation, and water. The land-cover map for the 1980s shows the highest vegetation percentage (42.5%), and the lowest urban (8.2%) and rural/urban-low-density (22.1%) percentages. We observe in the 1990s an increase in both urban (11.2%) and rural/urban-low-density (25.1%) areas, and a decrease in vegetation (36.3%). The numbers indicate the conversion of vegetation to both urban and rural/urban-low-density cover types. The land-cover map in the 2000s confirms a steady increase in the urban area (14.8%) and a decrease in the vegetated area (33.2%). Conversely to the 1990s, the rural/urban-low-density class decreased in the 2000s (24.6%), indicating the conversion of both vegetation and rural/urban-low-density classes to the urban one. Similar to the other decades, the urban and vegetation areas respectively increase (15.9%) and decrease (29.4%) again in the 2010s, whereas the rural/urban-low-density cover type increases (27.3%), reaching its highest value since the 1980s.

The maximum (minimum) vegetation cover occurs in the 1980s (2010s), and the urban and the rural/urban-low-density classes present the reverse evolution. The observed land-cover evolution confirms the urban expansion in MARJ over the last four decades.

Spatially, urban growth mainly occurs in western, northern, and eastern MARJ. There is a noticeable vegetation change to urban and rural/urban-low-density classes around the Mendenha's Mountain at the intersection of Rio de Janeiro with Itaguaí, Seropédica, and Nova Iguaçu municipalities. In the north, the development of Duque de Caxias, Magé and Guapimirim cities is expressive. COMPERJ has brought rapid economic growth in Itaboraí city in the MARJ's western region, following urban growth at an unparalleled scale and rate. Therefore, urbanization and new industrial spaces are responsible for the current transformations in the use of metropolitan land.

The MARJ urban spaces grew in three different moments in time. The western sector of Guanabara Bay and the Tijuca massif surrounding areas are the oldest and most dense urban spaces (Guanabara's lowlands). Later, the urban area expanded towards the westerly direction, crossing the lowlands of Bangu, Jacarepaguá, Santa Cruz, and Guaratiba, between the Pedra Branca and Mendenha massifs. Most recently, the urban expansion occurred towards the eastern sector of Guanabara Bay, encompassing Niterói, São Gonçalo, and Itaboraí cities, as well as towards the north of the Guanabara's lowlands, including different cities forming the Baixada Fluminense region. Both locations are areas with mixed land-use exhibiting urban, rural, and vegetated (original forest within conservation units) landscapes.

Inside the Rio de Janeiro city, we observe an expressive vegetation conversion to urban areas around Pedra Branca and Tijuca's mountains. The west side of the Rio de Janeiro city also shows accelerated urban development near the Sepetiba's bay in the past few years, mainly due to the Itaguaí port complex's investments.

3.2. Heat fluxes characterization

Figs. 5–7 show the intra-annual variation of different parameters associated with urbanization for urban, rural/urban-low-density, and vegetation classes. We use box-plots to compare the different groups of data and land-covers throughout the year. The box-plots summarize each data distribution using the median, quartiles, and the lowest and highest data points.

Almost all parameters have higher values and variability in the summer than in the winter because the amount of solar radiation that reaches the surface depends essentially on the earth-sun relationship

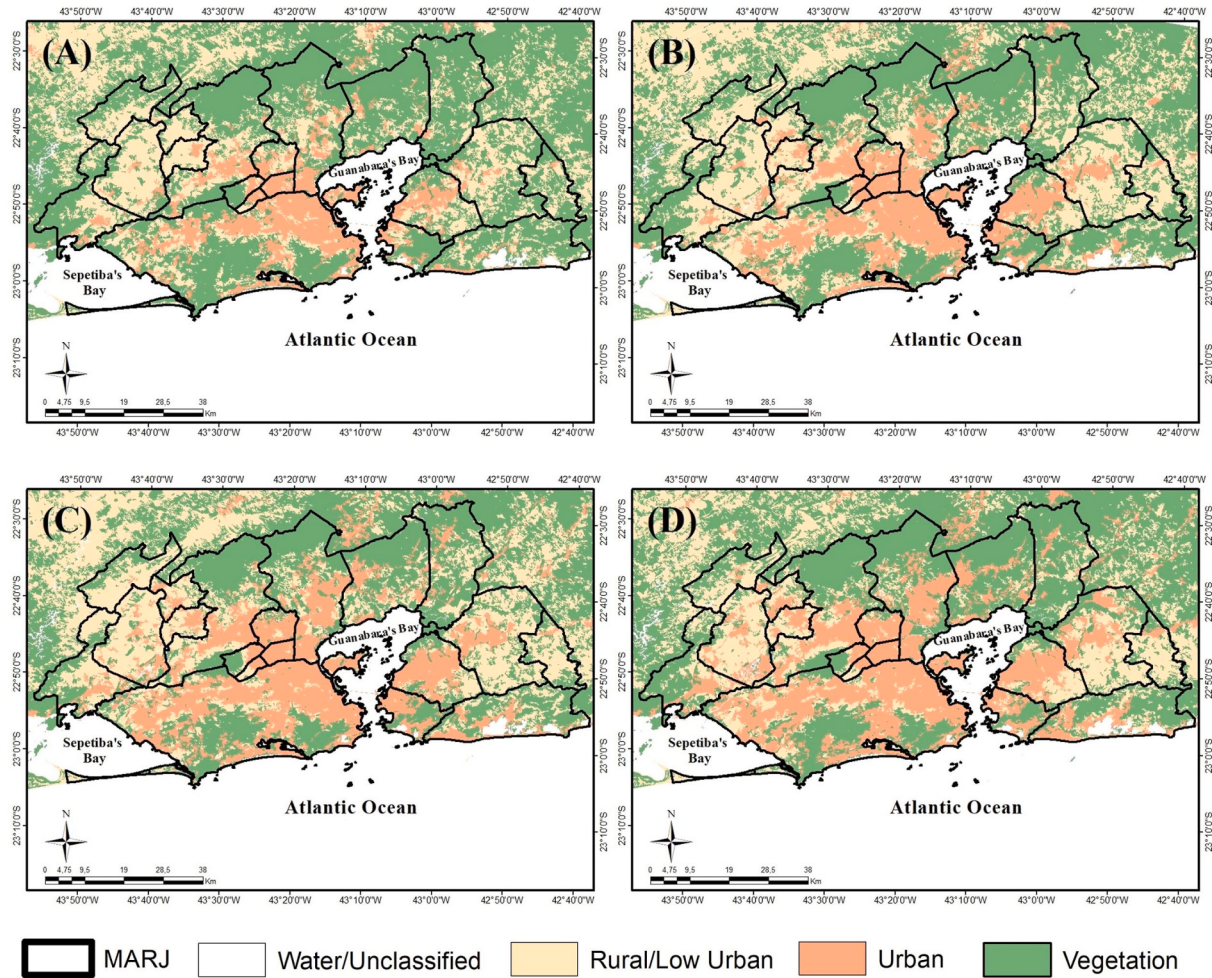


Figure 4. Land-cover maps for MARJ for the 1980s (a), 1990s (b), 2000s (c), and 2010s (d) decades. The classification considers four classes: urban (orange), rural/urban-low-density (yellow), vegetation (green), and water (white). (For interpretation of the references to colour in this figure legend, the reader is referred to the Web version of this article.)

and is higher in the summer.

As expected, neither NDVI (median around 0.25) nor LAI (0.25) showed annual variation for the urban class (Fig. 5a and b), but they display a typical small seasonal variability of tropical vegetation for the vegetation class (NDVI from 0.65 to 0.55, and LAI between 2.5 and 1.25). The interclass comparison confirms the highest NDVI and LAI values for the vegetation class, whereas the LST (Fig. 5d) is always higher (lower) for the urban (vegetation) class stressing the SUHI phenomenon. The median LST value reached its maximum around of 310K (300K) in January and minimum around of 298K (293K) in June for the urban (vegetation) class.

Albedo shows a conspicuous pattern over MARJ with the highest (0.20–0.22) and lowest (0.15–0.17) median values occurring for urban and vegetation classes, respectively (Fig. 5c). Conversely, some studies report that city albedo values are habitually 2–5% lower than adjacent rural areas [60,61,62]. For instance, Jin et al. (1999) [62] compared urban and rural albedos between 30° and 65°N and showed that urban areas have lower albedo values than cropland and deciduous forests despite the observed intra-annual variations. Moreover, they proposed an urban index to distinguish urban surfaces from natural ones based on such behavior.

We have also compared the obtained albedo from the weighted mean of the reflectances in Landsat bands with the MODIS albedo product (MCD43C3) over MARJ since the MODIS algorithm is capable of accurately characterizing land-surface albedo by using multiday, multiband,

atmospherically corrected cloud-cleared multiangular reflectance observations. Accordingly, we use the MCD43C3 product to compute the actual land-surface albedo as a weighted mean between the white-sky and black-sky albedos, based on the fraction of diffuse skylight (a function of aerosol optical depth, aerosol type, solar zenith angle, and band). Then we have characterized the albedo of vegetated and urban surfaces using the MODIS land-cover product (MCD12C1). The MODIS values corroborate the results from Landsat data showing that the urban area over MARJ has a higher mean albedo value (0.15 for the urban and built-up class) than the adjacent vegetated surfaces (values varying from 0.11 to 0.13 for different vegetation classes). Although the absolute Landsat and MODIS albedo values differ, the relative difference between urban and vegetation classes is almost the same.

Such results from both Landsat and MODIS data reflect the different radiative properties of human-made materials, indicating a bright impervious surface over MARJ (e.g., concrete and high reflectance roofs) rather than a dark one, composed of roads, asphalt, and dark building roofs. Therefore, the albedo of the urban constructions over MARJ seems, in general, compared to the vegetation, not to be an additional contributing factor to the UHI.

Fig. 6 (a-d) explores the pattern of the four components of the surface radiation balance. All components show a marked intra-annual variation with higher values in the summer following solar radiation throughout the year. For instance, the downwelling shortwave (longwave) radiation varies from 550 to 950 Wm⁻² (325–365 Wm⁻²). Both downwelling

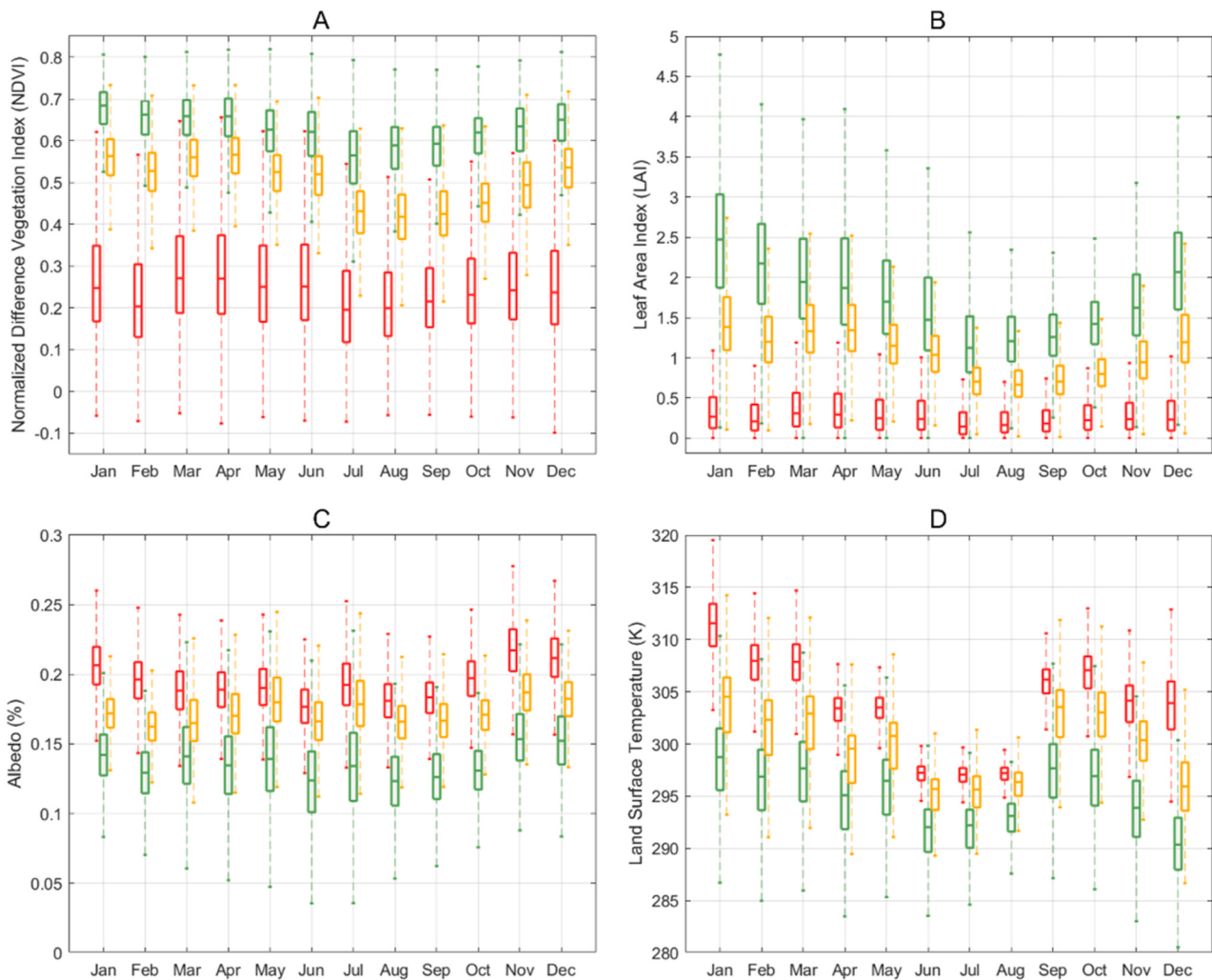


Figure 5. Monthly boxplots for NDVI (a), leaf area index (b), albedo (c), and land-surface temperature (d) in urban (red), rural/urban-low-density (yellow), and vegetation land-cover classes. (For interpretation of the references to colour in this figure legend, the reader is referred to the Web version of this article.)

shortwave and longwave radiations (Fig. 6a and b) mainly depend on the atmospheric state rather than surface characteristics, and therefore the interclass variation is insignificant.

Since the downwelling shortwave does not show a noticeable interclass variation, the albedo is the main variable which modulates the upwelling shortwave (Fig. 6c). The vegetation and urban areas present the lowest ($75\text{--}150 \text{ Wm}^{-2}$) and highest ($100\text{--}200 \text{ Wm}^{-2}$) upwelling radiation values, respectively. MARJ shows interesting radiative properties, with the vegetated areas absorbing more solar radiation than the urban ones.

Both LST (Fig. 5d) and the upwelling longwave radiation (Fig. 6d) shows the same intra-annual and interclass variations with the highest values in summer and urban class (500 Wm^{-2}) and the lowest in winter and vegetation (390 Wm^{-2}). On the other hand, the upwelling longwave median value for winter (summer) and urban (vegetation) class is 425 Wm^{-2} (430 Wm^{-2}). Since the upwelling longwave radiation depends on LST and broadband surface emissivity, this relationship standard is already expected.

Finally, Fig. 7 shows the intra-annual and interclass variability for the net radiation (a), ground heat flux (b), sensible heat flux (c), and latent heat flux (d). Since the downwelling radiations depend on the atmospheric state, then the albedo and LST ultimately determine the net radiation (Fig. 7a) differences among the land-cover classes. The vegetation (urban) class on MARJ has the lowest (highest) albedo and LST

and, accordingly, exhibits the highest (lowest) values of net radiation. These values vary from 400 Wm^{-2} (350 Wm^{-2}) in winter to 700 Wm^{-2} (500 Wm^{-2}) in summer for the vegetated (urban) area.

The ground heat flux empirically depends on NDVI, albedo, LST, and net radiation. Comparing the urban with the vegetation class (Fig. 7b), the former has greater ground heat flux values due to its lower NDVI and higher albedo and LST, even with its lower net radiation. Quantitatively, the ground heat flux for the urban (vegetation) class varies between 40 Wm^{-2} (30 Wm^{-2}) in winter and 100 Wm^{-2} (60 Wm^{-2}) in summer.

Fig. 7c depicts vegetation's critical role in maintaining lower and almost constant sensible heat flux throughout the year. The median value is around 100 Wm^{-2} and 3–3.5 times smaller than the summer's urban values. The difference between them drops 1.5–2 times during the winter, reinforcing the importance of vegetation in mitigating UHI in the hottest months of the year. Conversely, the urban median values vary from 150 Wm^{-2} in winter to 350 Wm^{-2} in summer.

Finally, the latent heat flux (Fig. 7d) shows the reverse sensible heat flux behavior with the urban class presenting, on the one hand, the lowest and constant numbers throughout the year ($150\text{--}200 \text{ Wm}^{-2}$). On the other hand, the vegetation depicts the highest median values characterized by a marked intra-annual variation with values around 600 Wm^{-2} and 300 Wm^{-2} in summer and winter.

We observe that 78% (69%) of the net radiation over vegetation is converted into latent heat flux in summer (winter), whereas 14% (23%)

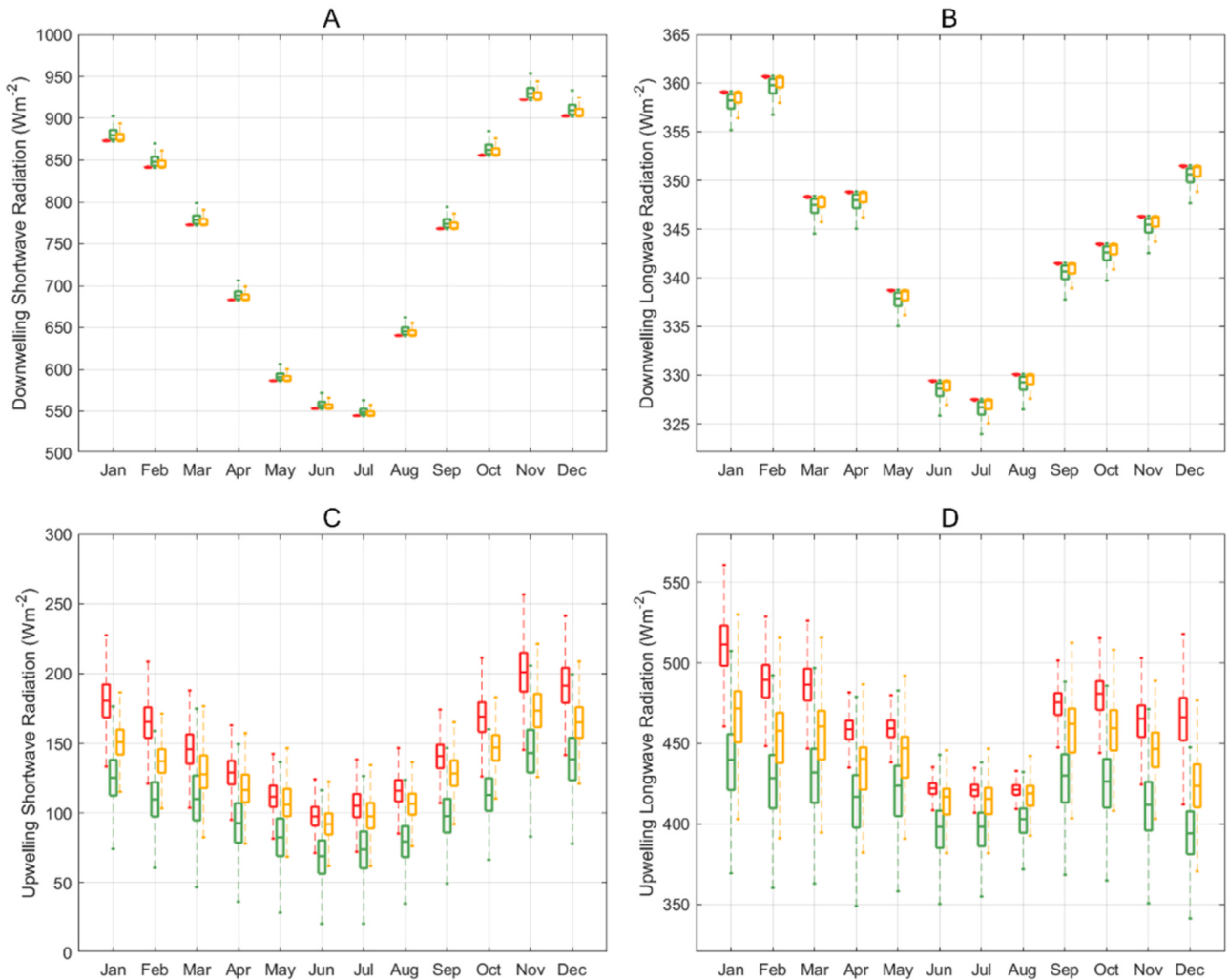


Figure 6. As in Fig. 5, but for downwelling shortwave radiation (a), downwelling longwave radiation (b), upwelling shortwave radiation (c), and upwelling longwave radiation (d).

and 8% (8%) into sensible and soil heat flux, respectively. The fraction of ground heat is almost the same for both seasons, and the fraction of latent heat flux is more significant in summer because the moist availability is higher in summer. Accordingly, the reverse occurs with the sensible heat flux, and it is only one-seventh of the available energy in summer. In contrast, the urban surface partitioned the energy into 30% (42%) of latent heat flux, 55% (45%) of sensible heat flux, and 15% (12%) of ground heat flux in summer (winter).

We computed the Bowen ratio to resume the MARJ climatic and surface characteristics respecting the energy partitioning. It was generally positive, and both fluxes are away from the surface. Such characteristics are typical during daytime conditions when the Landsat acquisition occurs (around 10:00 a.m. local time).

The seasonal variation shows a small increase of the Bowen ratio at the vegetation class in winter (0.3) compared to the summer (0.2). Regardless, vegetation always presents sufficient water, and the latent heat flux dominates the energy partitioning, mainly in summer. The Bowen ratio value less than unity indicates a relatively cold and moist condition for the vegetated areas.

The urban surface also shows an intra-annual variation, but the winter value of the ration (1.1) is lower than the summer one (1.5). In both seasons, the Bowen ratio is greater than unity, and therefore the sensible heat flux dominates the energy partitioning, mainly in summer. Such values show that the urban area over MARJ is arid, where the

water is a limiting factor for evaporation, and the microclimate is dry and warm.

Fig. 8 displays the MARJ energy balance fluxes climatology's spatial distribution for austral summer (DJF) and winter (JJA), covering the variability throughout the year. The spatial contrast between urban and vegetation surfaces are visible for all energy balance components, mainly during the summer, enhancing the importance of the urban vegetation in maintaining the surface cooler and its role in mitigating the urban thermal discomfort, heatwaves [63], and cooling energy use.

Despite the season, the MARJ natural spaces concentrate the highest net radiation and latent heat flux values. Such spaces encompass the mountainous and forested relief of the northern portion (Serra Hills), the coastal massifs of Tijuca, Mendenha, and Pedra Branca, areas around the eastern coastal lagoons, fragments of mangrove to the north of Guanabara Bay, and additional vegetated areas in the far west. On the other hand, the MARJ urbanized spaces have the highest ground and sensible heat flux values.

The net radiation values range from 400 Wm⁻² to 500 Wm⁻² (300 Wm⁻² to 400 Wm⁻²) over the natural (urban) spaces in winter (Fig. 8a). In summer, the net radiation reaches values between 600 Wm⁻² and 800 Wm⁻² (500 Wm⁻² and 600 Wm⁻²) (Fig. 8b).

Regarding the ground heat flux, the urbanized lowlands show values between 41 Wm⁻² and 60 Wm⁻², and the massifs and Serra Hills have values between 20 Wm⁻² and 40 Wm⁻² (Fig. 8c). The contrast between

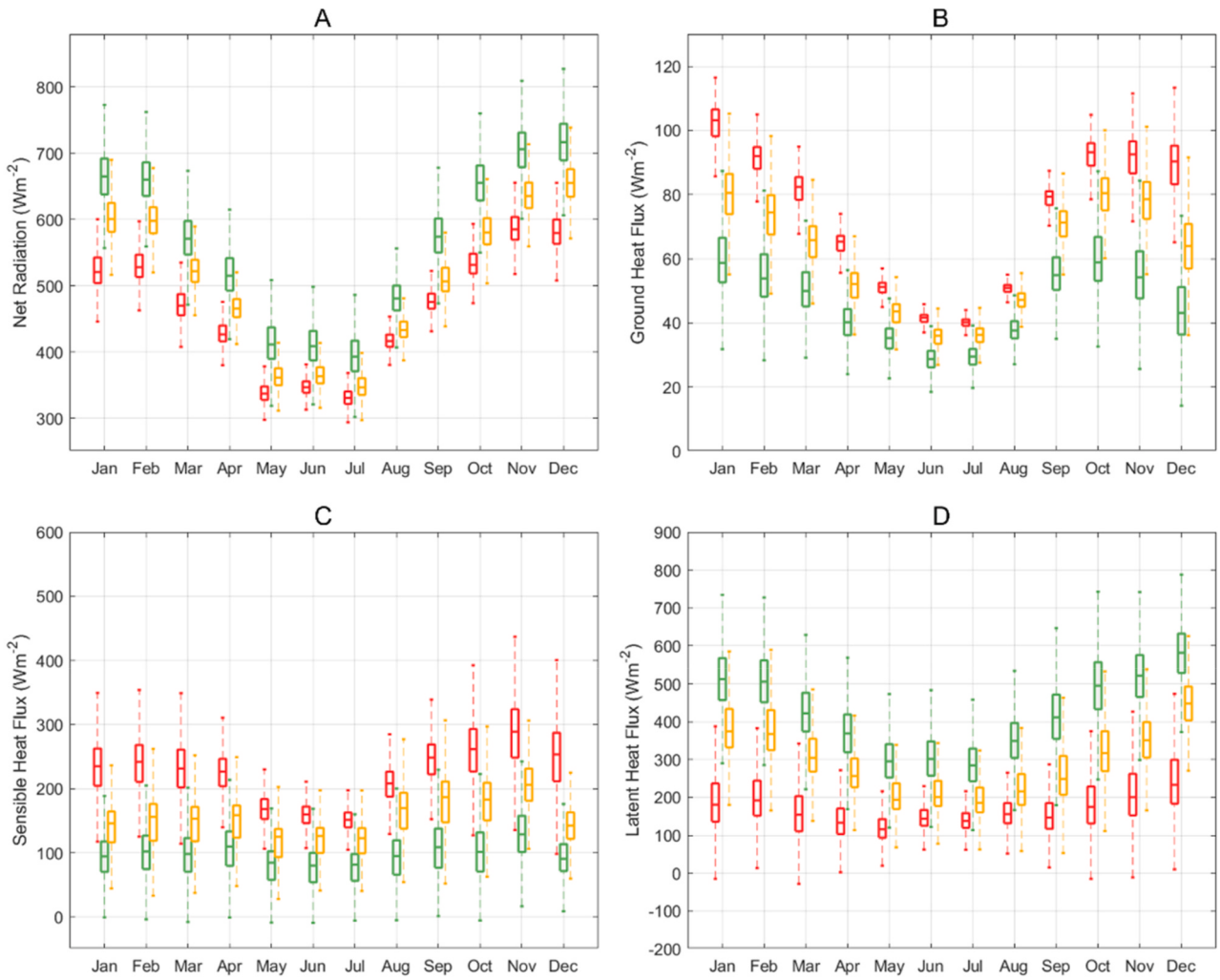


Figure 7. As in Fig. 5, but for net radiation (a), ground heat flux (b), sensible heat flux (c), and latent heat flux (d).

these natural and human-made features is most straightforward in summer (Fig. 8d) when the urban lowlands show the highest values (70 Wm⁻²-100 Wm⁻²), and the natural spaces show values between 20 Wm⁻² and 70 Wm⁻².

Fig. 8e and f shows a more segmented spatial variation of the sensible heat flux despite the season. The lowest values occur in the Sierra Hills (up to 50 Wm⁻²), coastal massifs (50 Wm⁻² -100 Wm⁻²), and lowland vegetated areas (100 Wm⁻² -150 Wm⁻²). It is worth noting that natural space values are almost the same in winter and summer, which do not happen for the urban spaces. Besides, we observe differences in urban values according to the urbanization level. The two more recent urbanized spaces show lower values (100 Wm⁻² -150 Wm⁻²) than the oldest and most dense urban one (150 Wm⁻² -200 Wm⁻²). The difference between them is 50 Wm⁻² for both seasons, and the summer values are 50 Wm⁻² higher than the winter ones. Resuming the results for the sensible heat flux, the more contemporary urbanized spaces have values around 100-150 Wm⁻² (150-200 Wm⁻²) in winter (summer), whereas the oldest urbanized spaces have values around 150-200 Wm⁻² (200-250 Wm⁻²).

The spatial contrast between natural and urbanized spaces are also clearly observed for the latent heat flux, but the former presenting the highest values and the latter showing the lowest ones. The natural spaces exhibit seasonal differences with values around 250-400 Wm⁻² in winter and above 450 Wm⁻² in summer. On the other hand, the MARJ lowlands' urban spaces do not reveal a substantial difference between winter and summer, with both seasons showing minimal values. Despite

the non-seasonal changes, the oldest and more urbanized space has lower values (0-150 Wm⁻²) than the less urbanized one (150-200 Wm⁻²).

We observe that the spatial pattern of heat fluxes follows the process of MARJ's urban consolidation, with the oldest and most dense urban spaces showing higher ground and sensible heat flux values than the more contemporary urbanized spaces. And the opposite for the latent heat flux. This urban transition space deserves continuous monitoring to analyze how future land-cover changes will affect the heat fluxes and then the UHI.

Fig. 9 shows the monthly UEBI intensity values respecting H, LE, Rn, G, and LST, computed from the difference between (\underline{EB}_u) and (\underline{EB}_v), and between (\underline{EB}_u) and (\underline{EB}_r). All differences were confirmed at a 1% significance level by both parametric Student's t-test and non-parametric Mann-Whitney-Wilcoxon rank-sum-test. The tests' power depends on the sample size, and the resulting statistical significance may be meaningless as the urban, vegetation, and rural/urban-low-density samples are huge ($n > 10,000$). Thus, we have randomly sampled 50 elements from the initial datasets and conducted the tests for these subsamples, according to Peres et al. (2018) [4]. The mean, standard deviation, and differences for the subsamples are virtually equal to those for the entire dataset.

We observe positive differences for H, G, and LST (higher values for the urban class), and negatives for LE and Rn (lower values for the urban class). The absolute urban-vegetation difference values are always

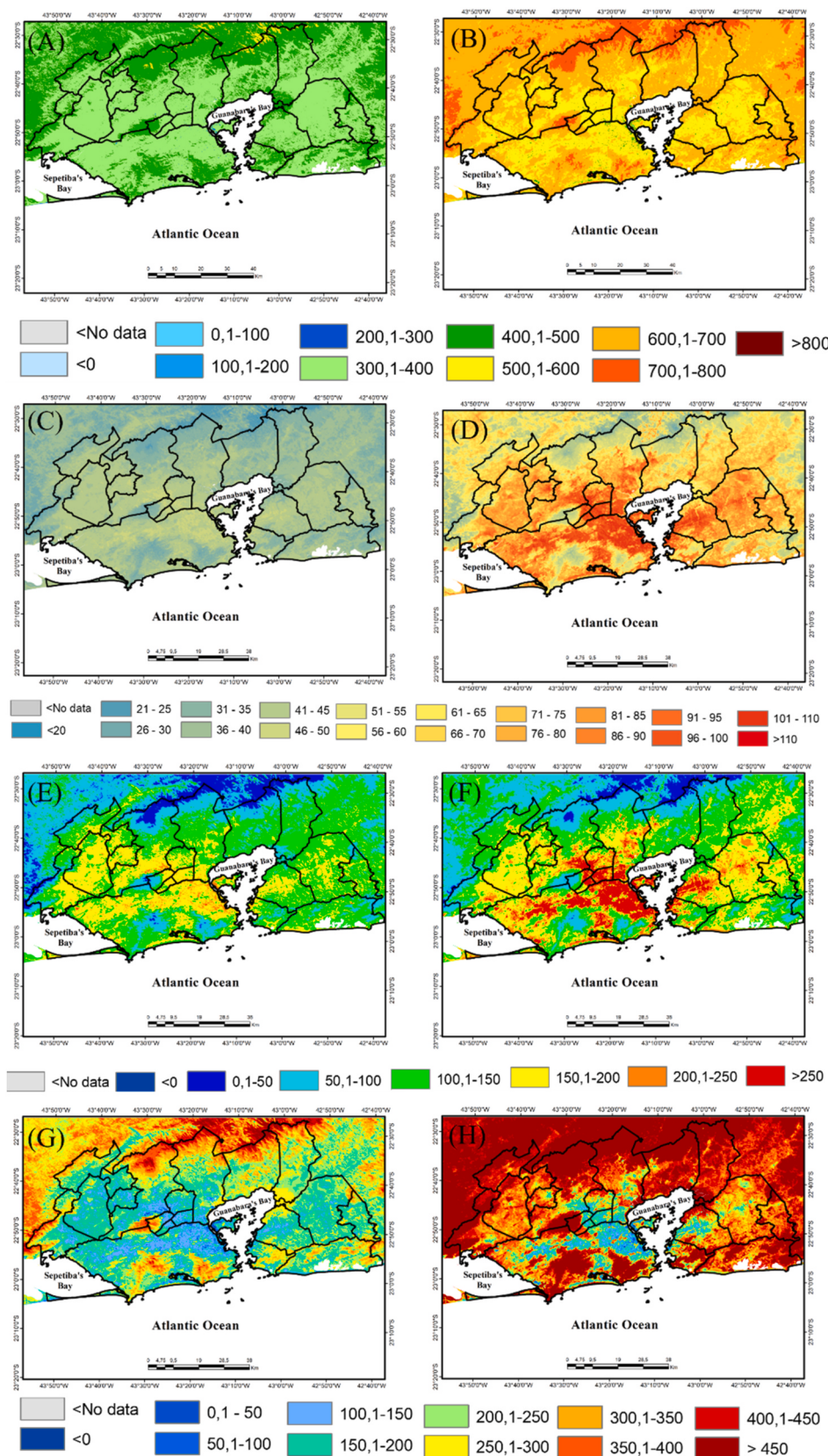


Figure 8. Spatial distribution of net radiation (a and b), ground heat flux (c and d), sensible heat flux (e and f), latent heat flux (g and h) for austral winter (JJAS) (left) and summer (DJF) (right), values are in Wm⁻² respectively.

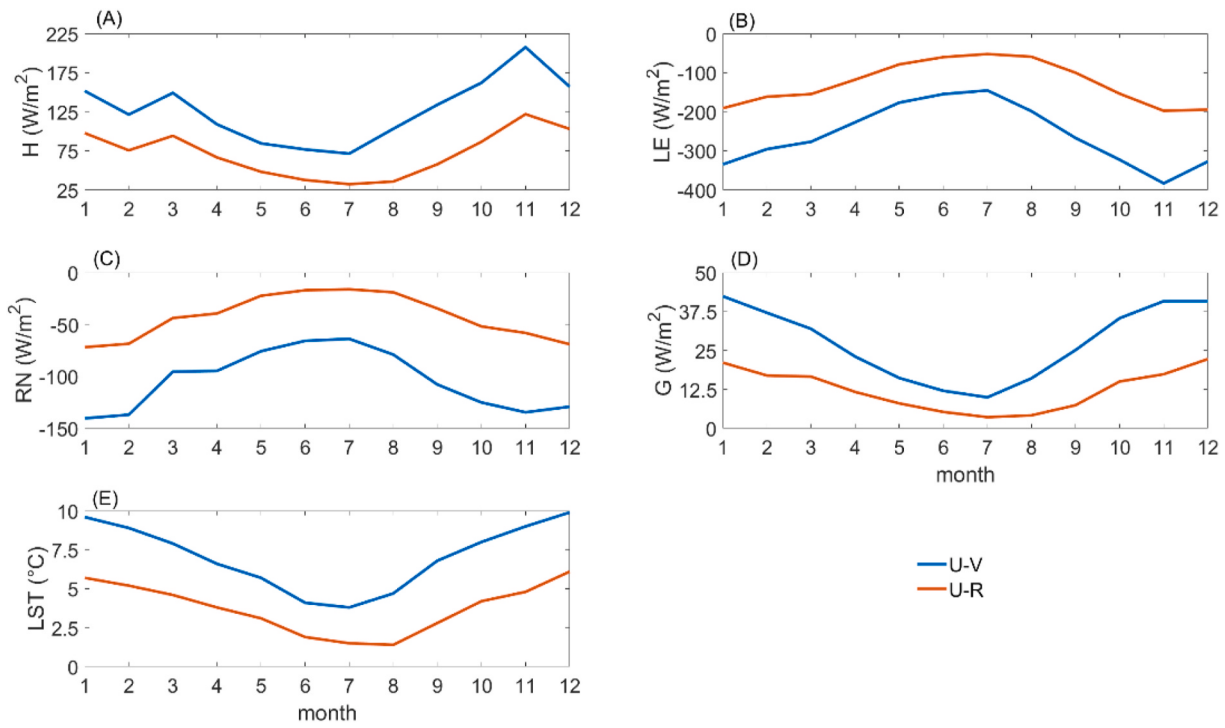


Figure 9. UEBI intensity monthly values for H (A), LE (B), Rn (C), G (D), and LST (E) for the differences between Urban-Vegetation (U-V) and Urban-Rural (U-R).

higher than the urban-rural/urban-low-density ones and always higher in summer than in winter. In general, the absolute UEBI intensity winter values are equal to half the summer ones. Although there is evident seasonal UEBI intensity variability, it is worth noting that H and LST (LE) are (is) low and almost the same throughout the year for the vegetation (urban) class.

Respecting LST, Peres et al. (2018) [4] have shown a UHI intensity between urban and vegetation (urban and urban-low-density) for 2000–2015 period of 7.1°C (4.4°C) using all available Landsat images together (irrespective of the month). However, the present study complements the information obtained by Peres et al. (2018) [4] by showing an intensity variability between urban and vegetation (urban and urban-low-density) from 3.8°C in July to 9.9°C in December (1.4°C in August to 6.1°C in December).

4. Conclusion

Our analysis using SEBAL and almost 40 years of Landsat-5, 7, and 8 data (1984–2020) show a steady advance of the urban areas in MARJ over the decades. By contrast, the vegetation coverage reaches its lowest value in the recent years. Previous studies focusing on temperate mid-latitudes cities have reported urban albedo values lower than the ones from adjacent rural areas, however, our results revealed an opposite behavior over MARJ, with the urban areas showing the highest values of albedo. Nevertheless, our results agree with recent global analysis [64]. The observed positive (negative) urban-vegetation albedo (net radiation) difference in MARJ contributes to reducing the UHI intensity, but this difference is not capable to compensate for the warming effects related to the partitioning of latent and sensible heat fluxes, and the soil heat flux. Such negligible compensation has been previously reported for wet regions [64]. Thus, the impermeable and less evaporative urban areas in MARJ have the highest values of land-surface temperature (sensible and soil heat fluxes) and define the UHI cores. Vegetation areas, on the other hand, demonstrate a great capacity to evaporate water and are the coolest spots in the MARJ.

Our results revealed that the UHI intensity in MARJ peaks during summer when the urban-vegetation temperature, sensible and latent

heat fluxes absolute differences reach maximum values around 9.9°C , 150 Wm^{-2} , and 330 Wm^{-2} . Such seasonal behavior is because the increase of the urban-vegetation difference in evapotranspiration cooling with water availability [64, 65]. Thus, we provide evidence that the UHI impacts on air quality, energy consumption and heat related mortality is highest in MARJ during the summer. This fact corroborates the results from Geirinhas et al. (2021) [63] which noted an enhancement of mortality rates during summer in MARJ due to heatwave occurrence. Those authors highlighted that UHI effect has a great potential for amplifying heat stress diseases over MARJ.

Although our study does not deal explicitly with the attribution of the urban-vegetation temperature difference and SEBAL computes the latent heat flux as a residual of the energy balance, the UHI intensity was previously demonstrated to be mainly controlled by the efficiency of urban and vegetation surfaces to evaporate water [65]. Therefore, our results showing a great urban-vegetation latent heat flux difference may indicate that the increase of green natural surfaces can reduce the UHI intensity in MARJ. Also, new methods used to understand the variations and the spatial distribution of the UHI, suggest that strategies enhancing the capability of surfaces to promote evapotranspiration are effective ways to mitigate the urban heat [65]. However, discussions around the quantification of such efficiency are still an opening chapter in UHI studies, especially for tropical and wet climate regions with precipitation $> 1000 \text{ mm yr}^{-1}$, such as MARJ. It has been shown that for wet regions such as tropical urban environments, where there are high values of precipitation, there is a larger requirement of extended green space to reduce the difference of temperature between urban and rural areas. Thus, a strategy based only on increasing the green areas would require the coverage of almost the entire city to compensate the much stronger effects of urbanization in wet climates due to the greater reduction of latent heat fluxes and evapotranspiration [64]. Even considering that vegetation has multiple benefits and services, the mitigation of the urban heat in MARJ may require to spend more efforts on original solutions.

Our study clear contributes to better understand the energy balance in tropical and wet climate urban areas by showing how urbanization affects the heat-energy fluxes on such climate conditions. However,

future urban studies on MARJ should be undertaken to accurately quantify the attribution of the UHI effect, namely the relative importance of evapotranspiration and convection efficiency, and to clarify how the background climate conditions in MARJ contribute to the UHI intensity variability. Moreover, the usage of a merge of different satellite systems (e.g., VIIRS, MODIS, ASTER, ABI) and a denser hydro-meteorological network to characterize urban land-atmosphere interactions may improve knowledge of UHI temporal and spatial variability in MARJ. It is worth mentioning that validation studies over urban regions should be continuously performed to ensure the reliability of remote sensing databases.

We are confident that our results and the above-mentioned further actions are critical for providing valuable and reliable information to decision-makers and stakeholders to design urban mitigation and adaptation plans for MARJ, and other Brazilian and South American cities as many of them are heat-uncomfortable and heavily populated with little or no trees, poor housing, and inadequate sanitation.

Fundings

This work was supported by the Fundação de Amparo à Pesquisa do Estado do Rio de Janeiro (FAPERJ) [grant numbers E–26/201.521/2014, E26/202.714/2019]; the Coordenação de Aperfeiçoamento de Pessoal de Nível Superior (CAPES) [master thesis grant]; and the Conselho Nacional de Desenvolvimento Científico e Tecnológico (CNPq) [grant number 311487/2021-1].

CRediT authorship contribution statement

Vitor Fonseca Vieira Vasconcelos de Miranda: Writing – original draft, Visualization, Software, Methodology, Formal analysis, Conceptualization. **Leonardo de Faria Peres:** Conceptualization, Formal analysis, Supervision, Writing – review & editing. **Andrews José de Lucena:** Writing – original draft, Supervision, Conceptualization. **José Ricardo de Almeida França:** Writing – review & editing. **Renata Libonati:** Writing – review & editing, Conceptualization.

Declaration of competing interest

The authors declare that they have no known competing financial interests or personal relationships that could have appeared to influence the work reported in this paper.

References

- [1] United Nations, World Population Prospects, Department of economic and social affairs. <https://population.un.org/wup/Publications/Files/WUP2018-Report.pdf>, 2018. (Accessed 15 March 2022).
- [2] A. Revi, D.E. Satterthwaite, F. Aragón-Durand, J. Corfee-Morlot, R.B.R. Kiunsi, M. Pelling, D.C. Roberts, W. Solecki, Urban Areas. Contribution of Working Group II to the Fifth Assessment Report of the Intergovernmental Panel on Climate Change, Climate Change 2014: Impacts, Adaptation, and Vulnerability. Part A: Global and Sectoral Aspects, Cambridge University Press, Cambridge, UK, 2014, pp. 535–612. https://www.ipcc.ch/site/assets/uploads/2018/02/WGII_AR5-Chap8_FINAL.pdf. (Accessed 17 March 2022).
- [3] United Nations Development Program, Human Development Report: beyond Income, beyond Averages, beyond Today, United Nations Development Program, 2019. <https://hdr.undp.org/sites/default/files/hdr2019.pdf>. (Accessed 15 March 2022).
- [4] L. de F. Peres, A.J. Lucena, O.C. Rotunno Filho, J.R.A. França, The urban heat island in Rio de Janeiro, Brazil, in the last 30 years using remote sensing data, *Int. J. Appl. Earth Obs. Geoinf.* 64 (2018) 104–116, <https://doi.org/10.1016/j.jag.2017.08.012>.
- [5] I.D. Stewart, T.R. Oke, Local climate zones for urban temperature studies, *Bull. Am. Meteorol. Soc.* 93 (2012) 1879–1900, <https://doi.org/10.1175/BAMS-D-11-00019.1>.
- [6] H. Akbari, S. Menon, A. Rosenfeld, Global cooling: increasing world-wide urban albedos to offset CO₂, *Clim. Change* 94 (2009) 275–286, <https://doi.org/10.1007/s10584-008-9515-9>.
- [7] X. Yang, Y. Li, The impact of building density and building height heterogeneity on average urban albedo and street surface temperature, *Build. Environ.* 90 (2015) 146–156, <https://doi.org/10.1016/j.buildenv.2015.03.037>.
- [8] K.W. Oleson, G.B. Bonan, J. Feddema, Effects of white roofs on urban temperature in a global climate model, *Geophys. Res. Lett.* 37 (3) (2010), <https://doi.org/10.1029/2009GL042194>.
- [9] N.O. Moraes, L.C.G. Pimentel, F.P. Duda, C. Silva, W.C.M. Farias, E. Marton, Use of atmospheric modeling for megacity urban planning: the case of temperature positive anomalies in the Rio de Janeiro metropolitan area, Brazil, *RA J. Appl. Res.* (2017) 1270–1287, <https://doi.org/10.18535/rajar/v3i12.04>.
- [10] R.L. Wilby, Constructing climate change scenarios of urban heat island intensity and air quality, *Environ. Plann. Plann. Des.* 35 (2008) 902–919, <https://doi.org/10.1068/b33066>.
- [11] H. Akbari, D. Kolokotsa, Three decades of urban heat islands and mitigation technologies research, *Energy Build* 133 (2016) 834–842, <https://doi.org/10.1016/j.enbuild.2016.09.067>.
- [12] M. Santamouris, A. Synnefa, T. Karlessi, Using advanced cool materials in the urban built environment to mitigate heat islands and improve thermal comfort conditions, *Sol. Energy* 85 (12) (2011) 3085–3102, <https://doi.org/10.1016/j.solener.2010.12.023>.
- [13] D.A. Quattrochi, M.K. Ridd, Measurement and analysis of thermal energy responses from discrete urban surfaces using remote sensing data, *Int. J. Rem. Sens.* 15 (10) (1994) 1991–2022, <https://doi.org/10.1080/01431169408954224>.
- [14] P. Shahmohamadi, A.I. Che-Ani, K.N.A. Maulud, N.M. Tawil, N.A.G. Abdullah, The Impact of Anthropogenic Heat on Formation of Urban Heat Island and Energy Consumption Balance, *Urban Studies Research*, 2011, pp. 1–9, <https://doi.org/10.1155/2011/497524>.
- [15] E.P. Marques Filho, H.A. Karam, A.G. Miranda, J.R.A. França, Rio de Janeiro's urban climate, *Urban Climate News—Quarterly Newsletter of the International Association of Urban Climate (IAUC)*, 32, 2009, pp. 5–9.
- [16] H.A. Karam, A.J.P. Filho, V. Masson, J. Noilhan, E.P.M. Filho, Formulation of a tropical town energy budget (t-TEB) scheme, *Theor. Appl. Climatol.* 101 (2010) 109–120, <https://doi.org/10.1007/s00704-009-0206-x>.
- [17] A.J. Lucena, O.C. Rotunno Filho, J.R. de A. França, L. de F. Peres, L.N.R. Xavier, Urban climate and clues of heat island events in the metropolitan area of Rio de Janeiro, *Theor. Appl. Climatol.* 111 (2013) 497–511, <https://doi.org/10.1007/s00704-012-0668-0>.
- [18] E.P. Marques Filho, A.P. Oliveira, W.A. Vita, F.L.L. Mesquita, G. Codato, J. Escobedo, M. Cassol, J.R.A. França, Global, diffuse and direct solar radiation at the surface in the city of Rio de Janeiro: observational characterization and empirical modeling, *Renew. Energy* 91 (2016) 64–74, <https://doi.org/10.1016/j.renene.2016.01.040>.
- [19] R.J.L. Flores, A.J. Pereira Filho, H.A. Karam, Estimation of long term low resolution surface urban heat island intensities for tropical cities using MODIS remote sensing data, *Urban Clim.* 17 (2016) 32–66, <https://doi.org/10.1016/j.ulim.2016.04.002>.
- [20] K. Fortuniak, An application of the urban energy balance scheme for a statistical modeling of the UHI intensity, in: Proceedings of the 5th International Conference on Urban Climate, 1, 2003. http://meteo.geo.uni.lodz.pl/icuc5/text/O_8_2.pdf. (Accessed 16 March 2022).
- [21] T.-W. Lee, J.Y. Lee, Zhi-Hua Wang, Scaling of the urban heat island intensity using time-dependent energy balance, *Urban Clim.* 2 (2012) 16–24, <https://doi.org/10.1016/j.ulim.2012.10.005>.
- [22] M.L. Imhoff, P. Zhang, R.E. Wolfe, L. Bounoua, Remote sensing of the urban heat island effect across biomes in the continental USA, *Remote Sens. Environ.* 114 (2010) 504–513, <https://doi.org/10.1016/j.rse.2009.10.008>.
- [23] M. Nogueira, S. Boussetta, G. Balsamo, C. Albergel, I.F. Trigo, F. Johannsen, D. Miralles, E. Dutra, Upgrading land-cover and vegetation seasonality in the ECMWF coupled system: verification with FLUXNET sites, METEOSAT satellite land surface temperatures, and ERA5 atmospheric reanalysis, *J. Geophys. Res. Atmos.* 126 (15) (2021), <https://doi.org/10.1029/2020JD034163>.
- [24] Y. Kodama, Large-scale common features of subtropical precipitation zones (the Baiu frontal zone, the SPCZ, and the SACZ) part I: characteristics of subtropical frontal zones, *J. Meteorol. Soc. Jpn.* 70 (1992) 813–836, <https://doi.org/10.2151/jmsj1965.70.4.813>.
- [25] A.M. Grimm, The El Niño impact on the summer monsoon in Brazil: regional processes versus remote influences, *J. Clim.* 16 (2003) 263–280, [https://doi.org/10.1175/1520-0442\(2003\)016-0263:TENIOT>2.0.CO;2](https://doi.org/10.1175/1520-0442(2003)016-0263:TENIOT>2.0.CO;2).
- [26] C.A.S. Coelho, C.P. de Oliveira, T. Ambrizzi, M.S. Reboita, C.B. Carpenedo, J.L.P. S. Campos, A.C.N. Tomaziello, L.A. Pamph, M. de S. Custódio, L.M.M. Dutra, R. P. Da Rocha, A. Rehbein, The 2014 southeast Brazil austral summer drought: regional scale mechanisms and teleconnections, *Clim. Dynam.* 46 (2016) 3737–3752, <https://doi.org/10.1007/s00382-015-2800-1>.
- [27] P. Satyamurti, C.A. Nobre, P.L. Silva Dias, Meteorology of the southern hemisphere, meteorological monographs, https://doi.org/10.1007/978-1-93504-10-2_5, 1998, 119–139.
- [28] L.M.V. Carvalho, C. Jones, M.A.F. Silva Dias, Intraseasonal large-scale circulations and mesoscale convective activity in tropical South America during the TRMM-LBA campaign, *J. Geophys. Res. Atmos.* 107 (2002) 1–20, <https://doi.org/10.1029/2001JD000745>.
- [29] H. Taha, Urban climates and heat islands: albedo, evapotranspiration, and anthropogenic heat, *Energy Build.* 25 (1997) 99–103, [https://doi.org/10.1016/S0378-7788\(96\)00999-1](https://doi.org/10.1016/S0378-7788(96)00999-1).
- [30] A.J. Arnfield, Two decades of urban climate research: a review of turbulence, exchanges of energy and water, and the urban heat island, *Int. J. Climatol.* 23 (2003) 1–26, <https://doi.org/10.1002/joc.859>.
- [31] M. Kanda, Progress in the scale modeling of urban climate: Review, *Theor. Appl. Climatol.* 84 (2006) 23–33, <https://doi.org/10.1007/s00704-005-0141-4>.

- [32] K. Zanter, Landsat 8 (L8) Data Users Handbook (Version 2.0). USGS, 33, Landsat Science Official Website, Virginia, USA, 2016. <https://www.usgs.gov/landsat-missions/landsat-8-data-users-handbook>. (Accessed 15 March 2022).
- [33] G. Camara, R. Cartaxo, M. Souza, U.M. Freitas, J. Garrido, Spring: integrating remote sensing and Gis by data modelling, *Science* 80 (20) (1996) 395–403, [https://doi.org/10.1016/0097-8493\(96\)00008-8](https://doi.org/10.1016/0097-8493(96)00008-8).
- [34] J. Storey, M. Choate, K. Lee, Landsat 8 operational land imager on-orbit geometric calibration and performance, *Rem. Sens. 6* (2014) 11127–11152, <https://doi.org/10.3390/rs6111127>.
- [35] J. Storey, D.P. Roy, J. Masek, F. Gascon, J. Dwyer, M. Choate, A note on the temporary misregistration of landsat-8 operational land imager (OLI) and sentinel-2 multi spectral instrument (MSI) imagery, *Remote Sens. Environ.* 186 (2016) 121–122, <https://doi.org/10.1016/j.rse.2016.08.025>.
- [36] P. Scaramuzza, E. Micijevic, G. Chander, SLC gap-filled products. https://d9-wret.s3.us-west-2.amazonaws.com/assets/palladium/production/s3fs-public/atoms/files/SLC_Gap_Fill_Methodology.pdf, 2004. (Accessed 15 March 2022).
- [37] G.B. França, A.P. Cracknell, A simple cloud masking approach using NOAA AVHRR daytime data for tropical areas, *Int. J. Rem. Sens.* 16 (1995) 1695–1705, <https://doi.org/10.1080/01431169508954506>.
- [38] F. Chen, J. Dudhia, Coupling an advanced land surface-hydrology model with the Penn-State-NCAR MM5 modeling system. Part II: preliminary model validation, *Mon. Weather Rev.* 129 (2001) 587–604, [https://doi.org/10.1175/1520-0493\(2001\)129<0587:CAALSH>2.0.CO;2](https://doi.org/10.1175/1520-0493(2001)129<0587:CAALSH>2.0.CO;2).
- [39] D.P. Roy, M.A. Wulder, T.R. Loveland, C.E. Woodcock, R.G. Allen, M.C. Anderson, D. Helder, J.R. Irons, D.M. Johnson, R. Kennedy, T.A. Scambos, C.B. Schaaf, J. R. Schott, Y. Sheng, E.F. Vermote, A.S. Belward, R. Bindschadler, W.B. Cohen, F. Gao, J.D. Hippel, P. Hostert, J. Huntington, C.O. Justice, A. Kilic, V. Kovalevskyy, Z.P. Lee, L. Lymburner, J.G. Masek, J. McCorkel, Y. Shuai, R. Trezza, J. Vogelmann, R.H. Wynne, Z. Zhu, Landsat-8: science and product vision for terrestrial global change research, *Remote Sens. Environ.* 145 (2014) 154–172, <https://doi.org/10.1016/j.rse.2014.02.001>.
- [40] X. Yu, G. Xulin, W. Zhaocong, Land surface temperature retrieval from Landsat 8 TIRS—comparison between radiative transfer equation-based method, split window algorithm and single channel method, *Rem. Sens. 6* (10) (2014) 9829–9852, <https://doi.org/10.3390/rs6109829>.
- [41] J.A. Barsi, J.R. Schott, S.J. Hook, N.G. Raqueno, B.L. Markham, R.G. Radocinski, Landsat-8 thermal infrared sensor (TIRS) vicarious radiometric calibration, *Rem. Sens.* 6 (11) (2014) 11607–11626, <https://doi.org/10.3390/rs6111607>.
- [42] F. Wang, Z. Qin, C. Song, L. Tu, A. Karnieli, S. Zhao, An improved mono-window algorithm for land surface temperature retrieval from landsat 8 thermal infrared sensor data, *Rem. Sens.* 7 (2015) 4268–4289, <https://doi.org/10.3390/rs70404268>.
- [43] Z. Qin, A. Karnieli, P. Berliner, A mono-window algorithm for retrieving land surface temperature from Landsat TM data and its application to the Israel-Egypt border region, *Int. J. Rem. Sens.* 22 (18) (2001) 3719–3746, <https://doi.org/10.1080/01431160010006971>.
- [44] J.C. Jiménez-Munoz, J.A. Sobrino, A generalized single-channel method for retrieving land surface temperature from remote sensing data, *J. Geophys. Res. Atmos.* 108 (2003), <https://doi.org/10.1029/2003jd003480>.
- [45] J.D. Souza, B.B. Silva, Correção atmosférica para temperatura da superfície obtida com imagem TM - landsat 5, *Rev. Bras. Geofís.* 23 (2005) 349–358, <https://doi.org/10.1590/S0102-261X2005000400002>.
- [46] A.A. Van De Griend, M. Owe, On the relationship between thermal emissivity and the normalized difference vegetation index for natural surfaces, *Int. J. Rem. Sens.* 14 (1993) 1119–1131, <https://doi.org/10.1080/01431169308904400>.
- [47] W.G.M. Bastiaanssen, M. Meneti, R.A. Feddes, A.A.M. Holtslag, A remote sensing surface energy balance algorithm for land (SEBAL) 1. Formulation, *J. Hydrol.* 212–213 (1998) 198–212, [https://doi.org/10.1016/S0022-1694\(98\)00253-4](https://doi.org/10.1016/S0022-1694(98)00253-4).
- [48] R. Waters, R. Allen, W. Bastiaanssen, M. Tasumi, R. Trezza, Sebal. Surface Energy Balance Algorithms for Land. Idaho Implementation, Advanced Training and User's Manual Idaho USA, 2002.
- [49] A.R. Huete, A soil-adjusted vegetation index (SAVI), *Remote Sens. Environ.* 25 (3) (1988) 295–309, [https://doi.org/10.1016/0034-4257\(88\)90106-X](https://doi.org/10.1016/0034-4257(88)90106-X).
- [50] B. Rabus, M. Eineder, A. Roth, R. Bamler, The shuttle radar topography mission - a new class of digital elevation models acquired by spaceborne radar ISPRS, *J. Photogram., Remote Sens.* 57 (2003) 241–262, [https://doi.org/10.1016/S0924-2716\(02\)00124-7](https://doi.org/10.1016/S0924-2716(02)00124-7).
- [51] J.W. Rouse, R.H. Haas, J.A. Schell, D.W. Deering, Monitoring vegetation systems in the great plains with ERTS, in: Proc Third Earth Resources Technology Satellite-1 Symp, Greenbelt MD, 3, NASA, Washington, D.C, 1974, pp. 301–317. Available: <https://ntrs.nasa.gov/citations/19740022614>. (Accessed 15 March 2022).
- [52] P.V. Prasad, Vara, Statistical and Spectral Approaches to Automate Hot and Cold Pixel Selection for Surface Energy Balance Based Evapotranspiration Mapping, Ogallala Aquifer Program, 2012, pp. 1–4, final report.
- [53] C.A. Paulson, The mathematical representation of wind speed and temperature profiles in the unstable atmospheric surface layer, *Appl. Meteorol.* 9 (1970) 857–861, [https://doi.org/10.1175/1520-0450\(1970\)009<0857:TMROWS>2.0.CO;2](https://doi.org/10.1175/1520-0450(1970)009<0857:TMROWS>2.0.CO;2).
- [54] E.K. Webb, Profile relationships: the log-linear range, and extension to strong stability, *Q. J. R. Meteorol. Soc.* 96 (1970) 67–90, <https://doi.org/10.1002/qj.49709640708>.
- [55] V.F.V.V. Miranda, L.D.F. Peres, E.P. Marques Filho, J.R.A. França, Validation of the surface energy balance retrieved from remote sensing data for the metropolitan area of Rio de Janeiro (MARJ), in: IGARSS IEEE International Geoscience and Remote Sensing Symposium, 2018, pp. 1672–1675, <https://doi.org/10.1109/IGARSS.2018.8519424>.
- [56] A.P. Oliveira, E.P. Marques Filho, M.J. Ferreira, G. Codato, F.N. Dutra Ribeiro, E. Landulfo, G. de Arruda Moreira, M.M. Rocha Pereira, P. Mlakar, M.Z. Boznan, E. S. de Assis, D.G. Ferreira, M. Cassol, J.F. Escobedo, A.D. Pai, J.R.A. França, D. A. Quintão, F.D. Rabelo, L.A. Tolentino Souza, W.P. da Silva, L.M. Domingues, M. P. Sánchez, L.C. da Silveira, J.V. Vito, Assessing urban effects on the climate of metropolitan regions of Brazil - preliminary results of the MCITY Brazil project, *Explor. Environ. Sci. Res.* 1 (2020) 38–77, <https://doi.org/10.47204/eesr.1.1.2020.038-077>.
- [57] M. Cheng, X. Jiao, B. Li, X. Yu, M. Shao, X. Jin, Long time series of daily evapotranspiration in China based on the SEBAL model and multisource images and validation, *Earth Syst. Sci. Data* 13 (8) (2021) 3995–4017, <https://doi.org/10.5194/esd-13-3995-2021>.
- [58] Ying-ying Li, Hao Zhang, Wolfgang Kainz, Monitoring patterns of urban heat islands of the fast-growing Shanghai metropolis, China: using time-series of Landsat TM/ETM+ data, *Int. J. Appl. Earth Obs. Geoinf.* 19 (2012) 127–138, <https://doi.org/10.1016/j.jag.2012.05.001>.
- [59] J.L. Geirinhas, A. Russo, R. Libonati, P.M. Sousa, D.G. Miralles, R.M. Trigo, Recent increasing frequency of compound summer drought and heatwaves in Southeast Brazil, *Environ. Res. Lett.* 16 (3) (2021), 034036, <https://doi.org/10.1088/1748-9326/abe0eb>.
- [60] G. Manoli, S. Fatichi, M. Schläpfer, K. Yu, T.W. Crowther, N. Meili, P. Burlando, G.G. Katul, E. Bou-Zeid, Magnitude of urban heat islands largely explained by climate and population, *Nature* 573 (2019) 55–60, <https://doi.org/10.1038/s41586-019-1512-9>.
- [61] D. Li, W. Liao, A.J. Rigden, X. Liu, D. Wang, S. Malyshev, E. Shevliakova, Urban heat island: aerodynamics or imperviousness? *Sci. Adv.* 5 (2019) 1–5, <https://doi.org/10.1126/sciadv.aau4299>.